



Comparative Study on the Corrosion Performance of APS-, HVOF-, and HVAF-Sprayed NiCr and NiCrBSi Coatings in NaCl Solutions

Mervi Somervuori¹ · Tommi Varis² · Maria Oksa³ · Tomi Suhonen¹ · Petri Vuoristo²

Submitted: 9 September 2021 / in revised form: 18 March 2022 / Accepted: 18 March 2022 / Published online: 14 April 2022
© The Author(s) 2022

Abstract Corrosion performance of NiCr and NiCrBSi coatings produced by APS, HVOF, and HVAF was studied by electrochemical measurements and immersion tests in 0.5 and 3.5 wt.% NaCl solutions. In the electrochemical measurements, the NiCr coatings performed better than the NiCrBSi coatings. The effect of the coating process on the corrosion resistance of the material was significantly lower than that of the selected materials, NiCr or NiCrBSi. All the coatings showed a tendency to passivate but suffered from localized corrosion. During immersion exposure for ten weeks, localized corrosion appeared at heterogeneous areas of the coatings, including voids, defects, or powder particles that had not melted during the spraying process.

Keywords corrosion resistance · electrochemical measurements · immersion · Ni-based coatings · thermal spray

Introduction

Thermally sprayed Ni-based coatings are often used in applications where the components require protection from wear and corrosion. Such potential applications may include, for example, offshore hydraulic cylinders (Ref 1),

valves and heat exchangers (Ref 2) and pumps (Ref 3). The coatings can be applied to protect components as bond coats for other coatings or as a single layer coating. Seawater resistance of wrought nickel-based alloys, such as Inconel 625, has been proved to be excellent and is based on the protective Cr₂O₃ layer formed on their surface (Ref 4). The corrosion properties of thermally sprayed nickel-based alloys have been studied in several publications either in simulated seawater (Ref 5, 6) or 3.5% NaCl solution (Ref 7-11). The microstructure formation of thermally sprayed NiCr and NiCrBSi coatings and the influence of microstructure on corrosion properties are also widely published (Ref 6-9, 11-17). The publications related to the corrosion resistance of thermally sprayed coatings have concluded that the specific structure of thermally sprayed coatings affects the corrosion performance of coatings significantly. The main structural issue with thermally sprayed coatings is that they are not fully dense due to their porosity and imperfect lamella cohesion. The uneven distribution of the alloy constituents can also have a significant effect on the corrosion resistance of the coatings (Ref 5-20). It has been shown that the coating microstructure largely determines its saline corrosion performance and affects the corrosion mechanisms. Zhao et al. (Ref 11) showed that the most severe failure of HVOF-sprayed NiCrBSi coating resulted from peel off due to corrosion at the interface of the substrate and the coating. This mechanism requires penetration of corrosive media through the coating along the open routes immediately or over a more extended period due to selective corrosion of the coating. When corrosive media has penetrated the interface, corrosion of the base material can cause the coating to peel off. The density of defects such as unmelted particles, pores, inclusions, and microcracks in the microstructure of the coating can significantly affect the

✉ Mervi Somervuori
mervi.somervuori@saunis.net

¹ Sustainable products and materials, VTT Technical Research Centre of Finland, Espoo, Finland

² Faculty of Engineering and Natural Sciences, Tampere University, Tampere, Finland

³ Carbon neutral solutions, VTT Technical Research Centre of Finland, Espoo, Finland

rate of destruction of the coating. Thus, selective corrosion of coatings is more severe than for bulk materials. The coatings reduced corrosion performance compared to wrought materials having nominally similar composition that has been highlighted by Neville et al. (Ref 4) and Ahmed et al. (Ref 18). Neville et al. showed that the corrosion problems in HVOF-sprayed Inconel 625 coating are primarily due to local corrosion caused by the inhomogeneity of the coating, and they even stated that it could hardly be improved, e.g., by sealing treatment.

Different thermal spray processes, such as atmospheric plasma spraying (APS), high-velocity oxygen fuel (HVOF), and high-velocity air fuel (HVOF), produce different particle temperatures and velocities, which significantly affect the density, microstructure, and homogeneity of the thermal-sprayed coating (Ref 9, 13). Zhao et al. stated that corrosion performance might be improved by adjusting the HVOF process parameters (Ref 11). Sadeghimeresht et al. (Ref 9) showed by comparing the corrosion behavior of APS-, HVOF-, and HVAF-sprayed Ni, NiCr, and NiAl coatings, the electrolyte penetration into the dense HVAF coating was significantly reduced, which enhanced the corrosion resistance of the coating in 3.5% NaCl solution. Similar findings for cold-sprayed Ni-based coatings, which had dense and uniform microstructure, have been done by Koivuluoto et al. (Ref 21, 22). In the studies of passivation behavior of thermally sprayed Fe-based amorphous coatings, several authors have stated that the HVAF spraying can produce coatings, which have enhanced formation of a dense passive film and lower susceptibility of localized corrosion attack, which indicates a higher ability to withstand uniform corrosion (Ref 23–25). They stated that favorable oxidation behavior of HVAF coatings is due to the more homogenous coating and thus higher growth rate of the oxide layer with better protective property. A prerequisite for a homogeneous coating structure is that the microstructure of the powder is homogeneous. Furthermore, when a homogenous structure is desired, it is crucial that particle size distribution, which should be typically finer with HVAF than with HVOF, is suitable for the process. Based on various studies, it can be concluded that when corrosion barrier properties are required for the coating, it is desired that the material can passivate by forming a protective oxide layer and that the corrosion media cannot penetrate through the coating (Ref 8, 12, 13, 19, 20).

In this study, the corrosion behavior of NiCr and NiCrBSi coatings in 0.5 wt.% and 3.5 wt.% NaCl solution was addressed. Of these materials, NiCrBSi is a so-called self-fluxing or fusible alloy, which, when fused, forms a different microstructure compared to the coating in the as-sprayed state (Ref 26–30). Here, the coatings are studied in their as-sprayed condition. When considering the decline in

corrosion resistance due to the inhomogeneity of the coating as pointed by Ahmed (Ref 18) and Neville (Ref 4), it is crucial to consider the uniformity and microstructure of the powder before spraying and how the microstructure of the coating is formed during spraying depending on the alloying and thermal spray processing method. Therefore, powders with different melting points and microstructures were selected for this study. According to the powder manufacturer, Ni20%Cr has a melting point of 1400 °C and NiCrBSi 993 °C (fusing temperature). Furthermore, NiCrBSi alloy also contains carbon (C) and boron (B). Therefore, chromium carbides and chromium borides are formed in the Ni matrix (Ref 18, 27, 28). The matrix is a solid solution containing small amounts of Cr and Si (Ref 26). Carbides and borides increase the hardness of the coating but may affect the chromium distribution and thus the corrosion performance.

Coatings were applied using APS, HVOF, and HVAF processes. Different coating processes produce different thermal histories for the particles, resulting in a different microstructure. APS coatings were sprayed with the parameters recommended by the spray gun manufacturer. HVOF coatings were parameterized to emphasize coating tightness by selecting a spray gun configuration that has been found to produce fewer un-melted particles and gas-tight NiCr coatings by Oksa and Metsäjoki (Ref 31). In HVAF spraying of Ni-based materials, the powder is prone to clogging in the primary and secondary nozzles. To prevent this, Sadeghimeresht et al. (Ref 9), for example, used graphite nozzles and more recently, ceramic barrels have become available, which were used in this study. The spray parameters were optimized based on the principles described in several publications (Ref 9, 13, 20, 32). Particular attention was paid to differences in corrosion behavior between different TS processes and raw material properties. The main focuses were the effect of coating homogeneity on the passivation susceptibility and the effect of the differences on corrosion mechanisms. The coating corrosion behavior was studied by utilizing electrochemical measurements and immersion tests followed by SEM characterization.

Experimental

Spray Materials and Coating Manufacturing

The powders used for the studies were water atomized NiCr powders and gas atomized NiCrBSi powder from Oerlikon Metco, Switzerland. NiCr powders were Metco 43F-NS powder with the size distribution of 10–63 µm for APS and Metco 43VF-NS with the size distribution of 5–45 µm for HVOF and HVAF. NiCrBSi powder used for all the

processes was gas atomized Diamalloy 2001, which had a size distribution of 15–45 μm. The nominal compositions and the particle size distributions of powders are given in Table 1.

Coatings were sprayed with a ProPlasma APS plasma gun (Saint-Gobain, Avignon, France) connected to a Plasma-Technik A3000 system (Oerlikon Metco/Plasma-Technik, Switzerland), a Diamond Jet Hybrid 2700 HVOF (Oerlikon Metco AG, Wohlen, Switzerland), and an M3 HVAF (Uniquecoat Technologies LLC, Oilville, USA) processes. For the Saint-Gobain Pro plasma (APS), the parameters recommended by the manufacturer for the NiCr bond coating were used. For the DJ Hybrid (HVOF) process, the air cap 2702 was used with the parameters that were recommended for it. It should be noted that for Diamalloy 2001 powder and NiCr powders, the manufacturer recommended air cap 2701. However, this has been found in previous publications to produce high levels of un-melted particles in NiCr materials, which are highly undesirable as they prevent formation of liquid-tight coatings (Ref 31). Therefore, instead, a 2702 air cap was used. In HVAF M3 processes, the bases of the hardware and parameter selection can be found in (Ref 9). A pre-commercial ceramic 4L4C nozzle and a ceramic primary nozzle were chosen for the deposition to avoid powder build-up in the nozzles. In addition, a small combustion chamber was used to avoid powder clogging of the combustion chamber. The gun was adjusted close to maximum chamber pressure (approximately 97% of the maximum), because it is generally known that particle velocity increases with increasing chamber pressure. However, the maximum pressure is limited by the capacity of the air compressor. The fuel/air ratio of the M3 equipment was adjusted to ensure the stable burning of the flame. This adjustment range in the gun is relatively limited since it only works well over a relatively narrow range. The spray parameters used in this study are given in Table 2. The coatings for corrosion studies were deposited onto 150 x 50 x 5 mm size stainless steel AISI 316 steel plates, which were grit blasted using 500–700-μm corundum sand. A gun traverse speed of 0.9 m/s and a step width of 4 mm were used.

Characterization of Microstructure and Mechanical Properties

The microstructures of the coatings sprayed on S275 carbon steel substrates were investigated from cross-section samples that were mounted on resin and polished using conventional metallographic methods. These cross sections were characterized with a Zeiss ULTRA plus field-emission scanning electron microscope (Carl Zeiss AG, Oberkochen, Germany) using an accelerating voltage of 15 kV. ImageJ software was used for porosity analysis from backscattered electron micrographs. Porosities were measured over a 420 μm x 270 μm area from three different locations per coating. Coating Vickers hardness was measured on the polished surface using Struers Duramin-A300 (Struers ApS, Ballerup, Denmark) hardness testing machine with a load of 2.94 N (HV 0.3 kg). Ten indentations were performed on each coating. The as-sprayed surfaces of the specimens that were exposed to corrosive environment in the electrochemical measurements or the immersion test were studied after testing by optical microscope and characterized with scanning electron microscope (SEM). Elemental analysis of the coatings before and after corrosion tests were determined by energy dispersive x-ray spectroscopy (SEM ULTRA plus, Carl Zeiss, Oberkochen, Germany).

The viscous gas permeability tester, the principle of which is described in (Ref 33), was used to measure the gas flow through the as-sprayed coatings. Similar equipment was also used in the publications of Verstak et al. (Ref 34) and Oksa et al. (Ref 31, 35). In our case, the equipment is modified to produce pressures up to 10 bars and measure the flow with the 0.01 mL/min accuracy. Gas flow directly correlates with the coating through porosity. The principle of operation can be described as follows: (a) the test coating is applied onto a flat surface of a porous disk sample, (b) the sample is placed into the GPT-02 cell, (c) 99.9% nitrogen gas is delivered to the cell under the sample at a controlled pressure (max 10 bars), (d) the flow of gas through the coating is measured with a precise flow meter. The flows can be calculated as viscous permeability coefficient (ψ_v) by using the equation:

$$\Psi_v = 7783Q * \delta / \Delta P, \tag{Eq 1}$$

Table 1 Nominal compositions and particle size distribution of the powders

	Ni	Cr	B	Si	C	Fe	Mn	Others (max)	Particle size, μm
Ni20Cr	Bal.	19.5	...	1.2	...	0.25	0.25	0.5	10-63 (APS) 5-45 (HVOF and HVAF)
NiCrBSi	Bal.	17	3.5	4	1	4	15-45

Table 2 Spray parameters used for the deposition of coatings.

Spray device	SOD, mm	Current, A	Argon flow, L/min	Hydrogen flow, L/min	Carrier-Ar flow, L/min	Voltage, V	Power, kW
APS	120	500	55	8	4	72-73	36-37
	SOD, mm	Propane flow, L/min	Oxygen flow, L/min	Air flow, L/min	Carrier-N ₂ flow, L/min		
HVOF	250	70	238	375	20		
	SOD, mm	Propane 1 pressure, kPa	Propane 2 pressure, kPa	Air pressure, kPa	Carrier-N ₂ flow, L/min		
HVAF	300	758	689	786	60		

SOD stand-off distance

where Q is the flow rate, δ is the coating thickness, ΔP is the gas gauge pressure.

Corrosion Research Methods

The corrosion experiments were performed for the as-sprayed coatings. The substrate material was stainless steel AISI 316. The test specimens were cut from a coated plate. The cutting was performed in a careful manner by a method commonly used for thermal spray coatings. All uncoated areas of the specimens were masked with epoxy-tar paint (Teknotar 100, Teknos Oy, Helsinki, Finland). Thus, only the coated surface was exposed to the corrosive environment.

Electrochemical Measurements

The test specimens in the electrochemical measurements were 10 mm x 10 mm coupons with electrical contact via a wire joined at the back of the coupon. The exposed surface area was 1 cm². Before and after the measurement, the specimens were rinsed with ethanol (96%) and air-dried in warm air. The test specimens were photographed both before and after the measurement.

The corrosive environments for the electrochemical measurements were 0.5 and 3.5 wt.% NaCl solution. The experiments were performed at 21 °C using a simple three-electrode electrochemical cell where the electrodes were placed in a glass beaker with an electrolyte volume of 300 mL. The exposed surface of the working electrode was situated vertically, about 2 cm from the graphite bar that was used as a counter electrode. The reference electrode in the measurements was a saturated Ag-AgCl electrode (− 222 mV vs. SHE), but the results are presented here on the standard hydrogen electrode (SHE) scale. The electrochemical measurements were performed by potentiostat

Reference 600TM and its DC105 Framework software (Gamry Instruments, USA).

The electrochemical measurements were started with an open-circuit potential (OCP) measurement for one hour, and after that, a cyclic anodic polarization curve was measured. The specimen was polarized at a scan rate of 18 mV/min from the OCP to the anodic direction until the current density reached a current density of 5 mA/cm², and then the scan was reversed to the OCP.

The cyclic anodic polarization curves were used to compare the corrosion behavior of the coatings. Therefore, potential values were determined at current densities 1 and 2 mA/cm², and the pitting potentials were extrapolated from the curves.

Immersion Tests

Room temperature (21 °C) immersion tests of 10 weeks were performed for the coatings in 3.5 wt.% NaCl solution in sealed glass bottles. The size of the specimens was ca. 20 × 25 mm, and the coated area exposed to the corrosive media was ca. 3.5 cm². Two parallel specimens of each coating were used in the experiment, and each coating was placed into a separate bottle containing 0.5 l of electrolyte.

Characterization

The surfaces of the specimens used in the electrochemical measurements and the immersion tests were photographed by stereomicroscope both pre- and post-exposure. After the measurement, cross sections of some of the test specimens were made (Struers Tegramin, ground 220 grit, 500 grit and 1200 grit, polishing Largo 9 μm, Dac 3 μm, Mol 3 μm, Nap 1 μm). Cross sections were studied by scanning electron microscope coupled with an energy dispersive x-ray spectrometer (SEM/EDS, SEM ULTRApplus, Carl Zeiss, Oberkochen, Germany).

Results

Coating Microstructures and Mechanical Properties

The microstructures of the NiCr coatings are shown in Fig. 1 and NiCrBSi coatings in Fig. 2. The hardness, porosity, thickness, and viscous permeability coefficient of the coatings are given in Table 3.

The microstructures of the NiCr and NiCrBSi coatings shown in Fig. 1 and 2, respectively, differ with respect to the flattening of splats, the occurrence of oxides and the level of porosity. Concerning the NiCr APS coatings, the splats are well-flattened to form a clear lamellar structure, and the oxide strips are visible around lamellas. The higher porosity of APS coatings compared to HVAF- and HVOF-sprayed coatings is mainly due to the high amount of detachment between the lamellae. The high porosity lowers the hardness of the coating. The NiCr HVOF coating is very dense, showing the lowest porosity among all NiCr coatings. Lamellas are not very clearly visible, and the oxides occur as fragmented clusters. The porosity of the NiCr HVAF coating is more than 33% larger than the porosity of the NiCr HVOF coating. From Fig. 1, it seems evident that the porosity, which appears at the lamellae boundaries, is a result of the insufficient filling of splats. In this case, that was due to the insufficient degree of melting of powder particles related to the thermal energy of the spray hardware. A similar phenomenon is shown for HVOF spraying of NiCr (Ref 31). This can be avoided either by using a powder with a smaller maximum particle size or by increasing the thermal energy transferred to the particle by using a different gun configuration. However, in this case, ceramic nozzles other than 4L4 were not yet available.

In the NiCrBSi coatings, Fig. 2, due to B, Si, and C alloying, small precipitates of Cr carbides (such as Cr_7C_3 and $(\text{Cr}, \text{Ni})_{23}\text{C}_6$) and metal borides (such as CrB , $\text{Cr}/\text{Ni}_6\text{B}$, Ni_4B_3) can be seen in the structure (Ref 36). The precipitates have a clear effect on the coating hardness as shown in Table 3. These precipitates exist in the microstructure of

the powder. They are also seen in the coating, especially when the powder particles have not been completely melted, meaning that the precipitates could not dissolve in the matrix (Ref 36). There are several areas in the APS coating where the temperature of the powder particles was high enough to dissolve the original precipitates completely.

In contrast, precipitate dissolution occurred to a small extent at the outer edges of the lamellae of HVOF and HVAF coatings. The NiCrBSi APS coating has a slightly higher porosity than the NiCr APS coating, the NiCrBSi APS coating also contained globular pores, unlike NiCr APS coating. NiCrBSi HVOF and HVAF coatings are very dense, showing even lower porosity than NiCr HVOF and HVAF coatings. In these coatings, also clearly visible oxide clusters or bands are missing. Furthermore, significant differences in the amount of non-melted particles in the microstructure of NiCrBSi coatings compared to NiCr were observed. In NiCrBSi HVAF coating, a higher amount of non-melted particles were visible compared to NiCr HVAF coating. It seems obvious that with the parameters used, the lower melting temperature of NiCrBSi compared to NiCr is sufficient to increase the degree of melting of the larger particles and promote their attachment to the substrate.

Viscous gas permeability coefficient results show that such porosity that would allow nitrogen to flow through the coating was present only in the APS-sprayed NiCr coating. The other coatings were N_2 gas tight up to 10 bars pressure.

Results of Electrochemical Measurements

The measured open-circuit potentials (OCP) before the cyclic anodic polarization in 0.5 wt.% and 3.5 wt.% NaCl solution are shown in Fig. 3 and 4, respectively. Especially in the parallel curves measured for specimens of 0.5 wt.% NaCl solution, the variation can be remarkable, as shown in Fig. 3(c). However, in the stronger 3.5 wt.% NaCl solution, the potential curves of the similar specimens are almost equal, and for the APS coatings, the potential curves of

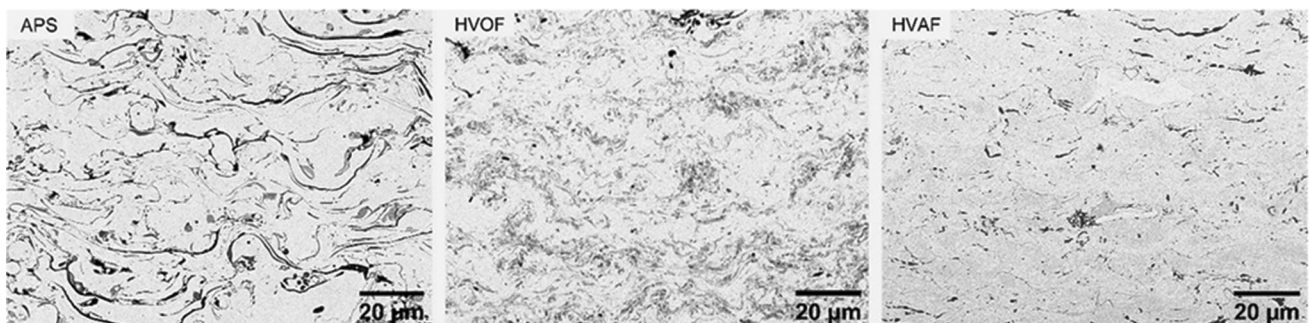


Fig. 1 Cross-sectional microstructures of the APS-, HVOF-, and HVAF-sprayed NiCr coatings imaged using scanning electron microscope with the backscatter detector (BSE)

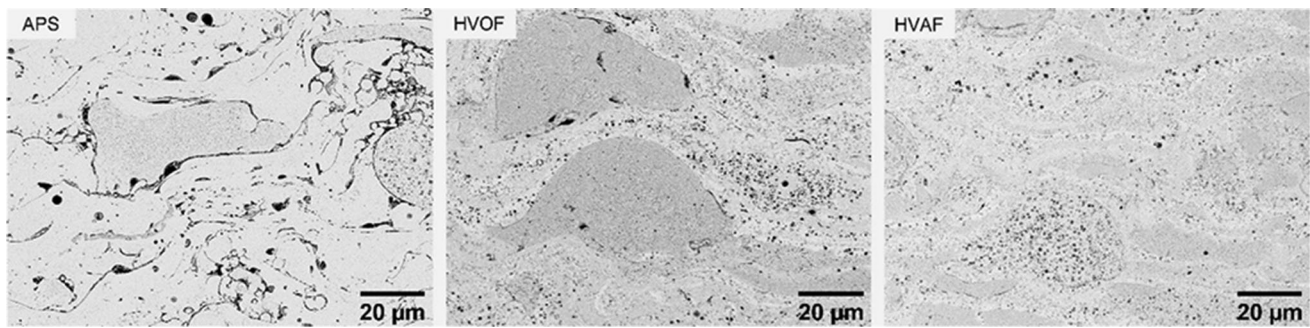


Fig. 2 Cross-sectional microstructures of the APS-, HVOF-, and HVAF-sprayed NiCrBSi coatings imaged using scanning electron microscope with the BSE detector

Table 3 Hardness, porosity, thickness, and viscous permeability coefficient of the coatings.

Material and spray method	Hardness HV, 0.3 kg	Porosity, %	Thickness, μm	Viscous permeability coefficient
NiCr APS	263 ± 34	1.5 ± 0.3	410	5.6 ± 0.4
NiCr HVOF	369 ± 17	0.6 ± 0.3	650	0
NiCr HVAF	366 ± 26	0.8 ± 0.1	500	0
NiCrBSi APS	562 ± 53	1.8 ± 0.4	490	0
NiCrBSi HVOF	637 ± 58	0.5 ± 0.2	340	0
NiCrBSi HVAF	642 ± 100	0.5 ± 0.4	350	0

parallel specimens are practically identical. The differences in the behavior between the parallel specimens are suspected to be due to the as-sprayed surfaces used in the measurements. Some rough profiles of the coatings are seen in the cross sections of the immersion tested specimens in Fig. 9–11. The surfaces of the thermal-sprayed coatings were not smooth, have porosity in the surface, and have heterogeneous microstructures. Therefore, they offer many sites where corrosion agents can infiltrate the coating. The porous and heterogeneous microstructures of the coatings are susceptible to form local corrosion microcells or are favorable sites for pitting corrosion. Nickel and chromium tend to passivate by forming protective oxide films, but inhomogeneity of the coating prevents the preservation of the protective oxide layer. For some coatings, potential variation is seen suggesting that the coating is passivating, but the passive film is being locally broken, e.g., by a pitting mechanism. It is also possible that the potential drop is caused by electrolyte penetration through the coating into the substrate, but the corrosion products seal the pathway formed. Strong potential drops, e.g., in the case of HVOF 0.5 NaCl in Fig. 3, could indicate this behavior.

Although there are differences in the OCP values, the cyclic anodic polarization curves measured in both NaCl solutions were more repeatable. The three measured

parallel curves for the specimens were quite similar. Figure 5 presents a typical polarization curve for each coating and the curve of the substrate AISI 316 measured in the same environment. The measurement direction of the curve is shown with an arrow in Fig. 5(a), and the dashed line shows the pitting potential value extrapolation from a measured curve.

In all curves of the coated specimens, the tendency for passivation is seen. However, the current rises and reduces at lower potentials than for the stainless steel specimens, which means that the corrosion resistance of the coated samples studied is not as good as that of stainless steel. There is a clear difference in the corrosion resistance of the NiCr and NiCrBSi coatings. The NiCr coating has a better corrosion resistance which can be seen from the lower current density at a particular potential. However, the effect of the three coating methods on corrosion resistance is not very easily seen from the curves. Therefore, the potential values at current densities of 1 and 2 mA/cm² and the pitting corrosion potential were determined from the curves. The results are in Fig. 6.

As expected, in the 3.5 wt.% NaCl solution, the measured corrosion currents are remarkably higher, and the current starts to rise at lower potentials than in the 0.5 wt.% NaCl solution. The smooth appearance of the curves measured for the coated specimens may indicate

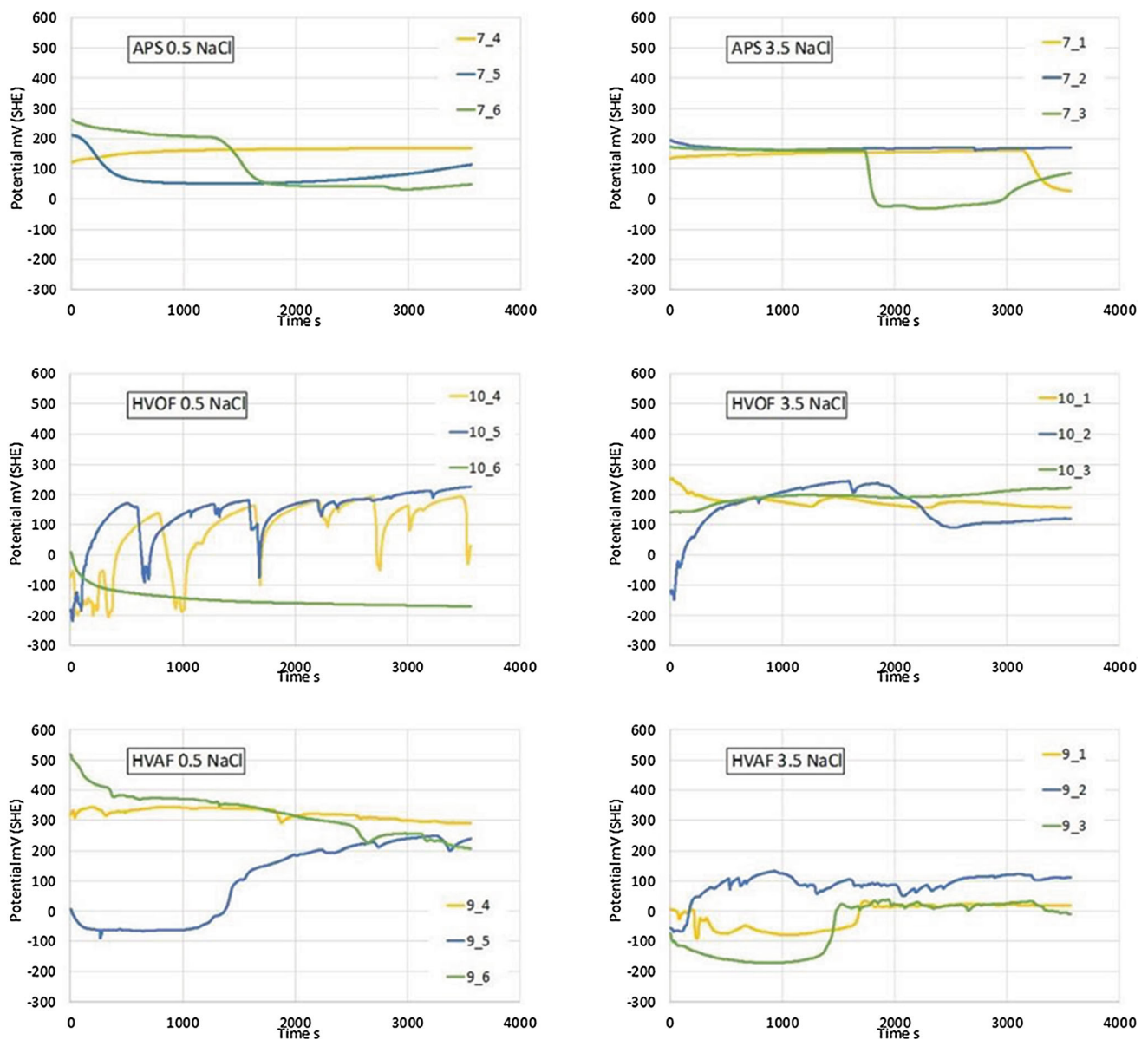


Fig. 3 OCP values of the NiCr-coated specimens measured in 0.5 and 3.5 wt.% NaCl solution before cyclic anodic polarization

stable growth of pits or other localized corrosion. For the stainless steel, the curves are not very smooth. They suffer from localized corrosion at high potentials, but the pits are re-passivated when the scan is reversed. In the 3.5 wt.% NaCl solution, the nonlinear form of the rising curve, i.e., a small elbow at about 2 mA/cm², may be an indication of the crevice corrosion found after the measurement between the protective paint and the stainless steel specimen.

In Fig. 6, it can be seen that the NiCr coatings are more corrosion resistant than the NiCrBSi coatings in the environments studied. Among NiCr coatings, the HVOF-sprayed coating is the best and the APS coating the poorest. However, in NiCrBSi coatings, the APS coating has the best corrosion resistance, but there is no significant

difference in the corrosion resistance of the HVAF and HVOF coatings.

Most of the measurements of the parallel specimens were quite well-repeatable. However, there were remarkable differences between the polarization curves of the NiCr coating produced by HVAF, as shown in Fig. 7. In one specimen, the corrosion resistance of the coated specimen was even better than that of the stainless steel substrate. This indicates that there may be significant differences in the corrosion performance of the coated specimens even when coated with the same material.

The surfaces of the coupons used in the electrochemical measurements were inspected visually and photographed by a stereomicroscope. In some specimens, the surface of

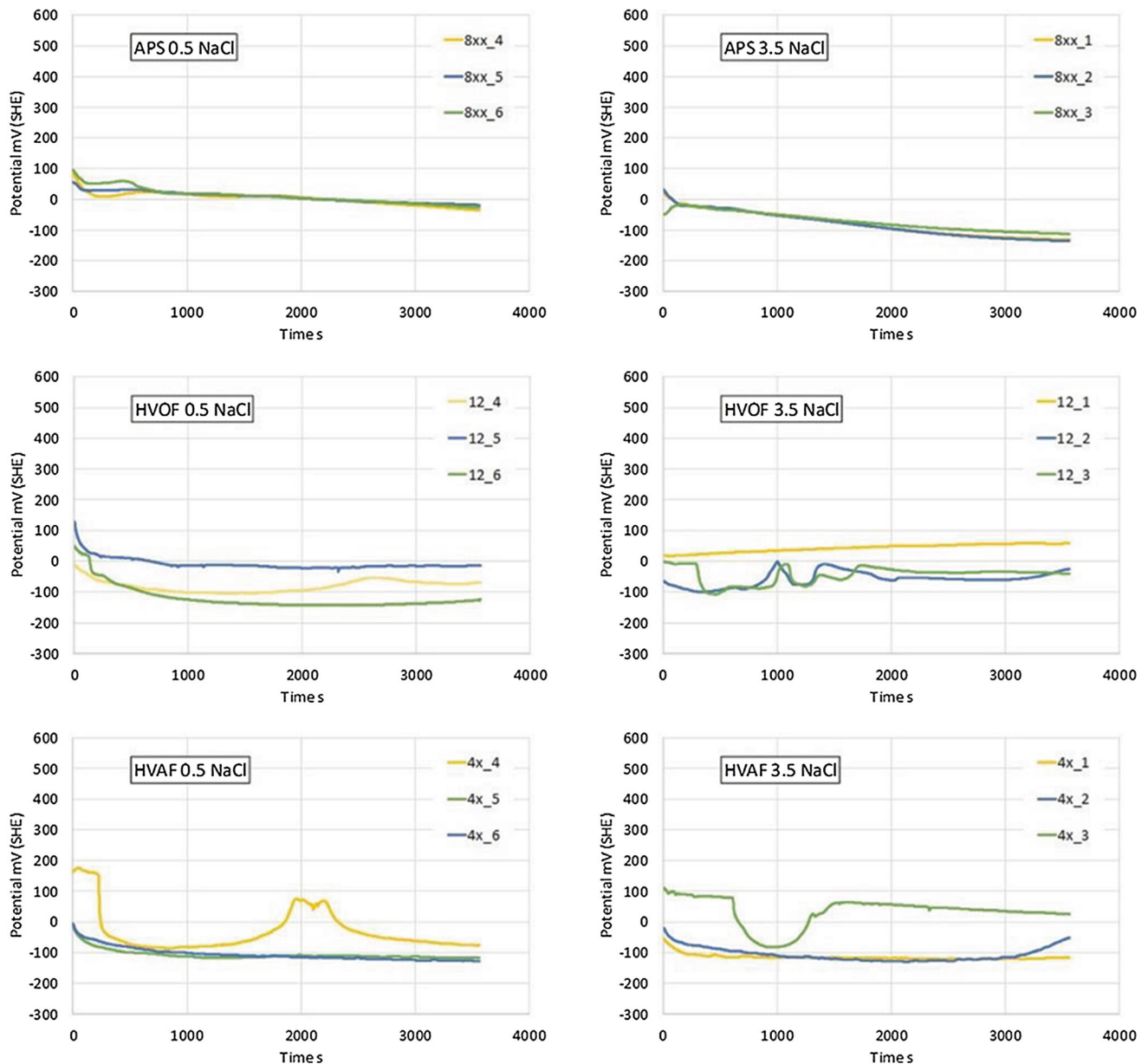


Fig. 4 OCP values of the NiCrBSi-coated specimens measured in 0.5 and 3.5 wt.% NaCl solution before cyclic anodic polarization

the coatings had turned slightly darker or partly lighter than the unexposed surface, and some specimens had some signs of corrosion products. However, stereomicroscope and SEM inspection showed only a few clear signs of corrosion on the surface. This is because the as-sprayed surfaces are rough and heterogeneous and contain various defects and voids. Therefore, it is hard to distinguish any minor signs of corrosion on the surface.

The cross sections of the specimens were studied with a stereomicroscope and an SEM. Signs of corrosion were found on the specimens tested in the stronger chloride solution. Figure 8 shows some cross sections of specimens following electrochemical measurements in 3.5 wt.% NaCl

solution. In all specimens, signs of corrosion were found near the outer surface of the coating. However, no signs of corrosion were found at the coating-substrate interface. In EDS analyses, some chlorine was found at the dark corroded areas and in some pores near the surface but not at the coating-substrate interface.

Immersion Test Results

After ten weeks of immersion in 3.5 wt.% NaCl solution, all specimens had some visible signs of corrosion. Therefore, all specimens were photographed by stereomicroscope, and one of the parallel test specimens of each

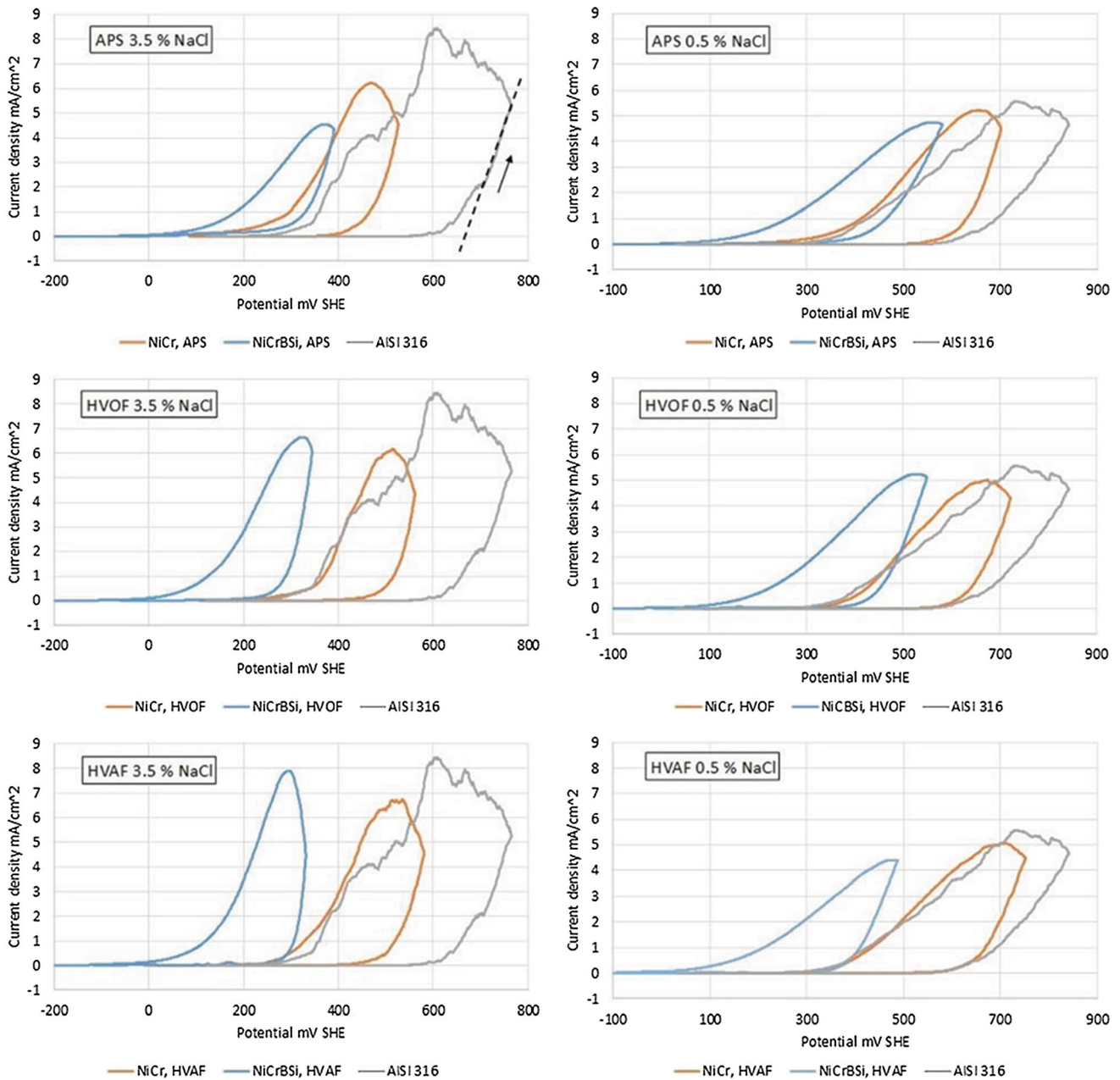


Fig. 5 Typical cyclic polarization curves of NiCr and NiCrBSi coatings measured in 3.5 wt.% and 0.5 wt.% NaCl solution compared to the curves of the stainless steel AISI 316 substrate material. The

arrow in (a) indicates the polarization direction, and the dashed line shows how the extrapolation of the pitting potential was made

coating was studied more closely by SEM. Images of the specimens are shown in Fig. 9, 10 and 11. There was visible corrosion on the surface of every specimen as can be seen on the stereomicroscope images of the specimens (Fig. 9a, c, and e, 10a, c, and e). However, not all specimens had clear signs of corrosion in the detailed cross section images taken by BSE SEM in (Fig. 11).

The non-flattened shape of the dark particles in NiCrBSi coating produced by HVAF (Fig. 11f) results from unmelted particles. The EDS maps in Fig. 12 show that the

particles are rich in chromium, but on the other hand, the iron and nickel content is reduced. Since no such significant differences in composition were observed in the EDS analysis of the as-sprayed coating, the change in composition is likely to be the result of selective corrosion of the un-melted particles.

The NiCr APS coating had a band of voids which result from spraying (Fig. 9b). However, only two of them were corroded during the immersion tests, and these two samples were studied more closely by SEM/EDS. The results in

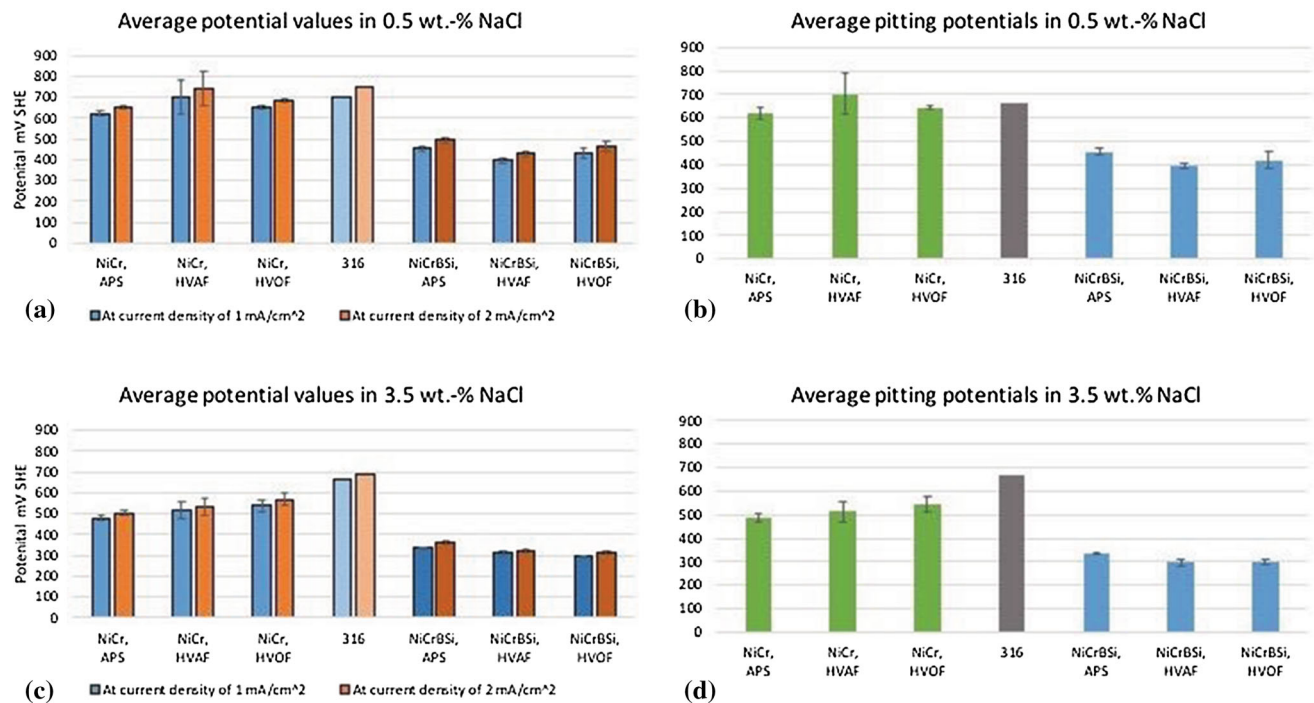


Fig. 6 Potential values (a) at current density 1 and 2 mA/cm² in 0.5 wt.% NaCl and (c) in 3.5 wt.% NaCl, and (b) extrapolated pitting potentials in 0.5 wt.% NaCl, and (d) in 3.5 wt.% NaCl

Fig. 7 Cyclic polarization curves of NiCr HVAF coatings and substrate AISI 316 measured in 0.5 wt.% NaCl solution

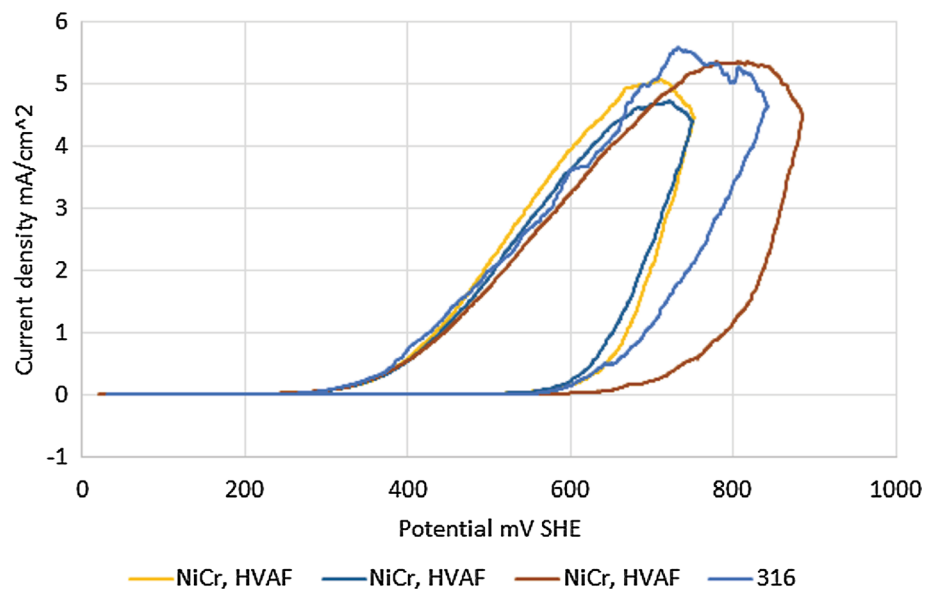


Fig. 13 show that some chlorine is present in the voids near the surface but not deeper in the coating. Sometimes such cone-shaped void bands, initiated from surface irregularities, may form in the coating during the deposition process. The analysis suggests that the pores are not interconnected and thus do not necessarily offer a route for the corrosive media to penetrate through the coating. The green corrosion product on the surface in Fig. 9(a) is mainly nickel oxide.

Discussion

Electrochemical methods, immersion tests and surface analysis were used to study corrosion of the sprayed NiCr and NiCrBSi coatings. The selected coating feedstocks for the study were atomized NiCr and NiCrBSi powders with solidus temperatures of 1400°C and 993°C, respectively. These powders were sprayed using three different processes APS, HVOF, and HVAF. Coating formation from

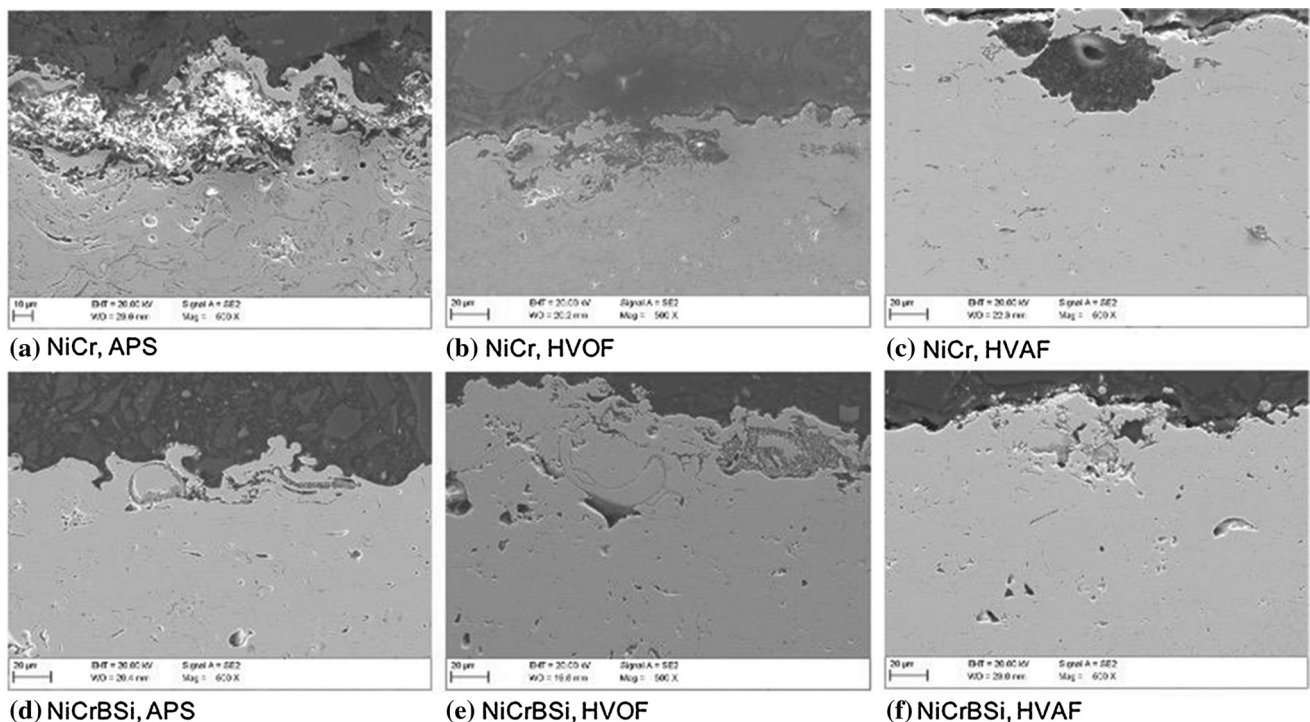


Fig. 8 SEM images of cross sections of the specimen after cyclic anodic polarization in 3.5 wt.% NaCl solution. (a) NiCr, APS, (b) NiCr, HVOF, (c) NiCr, HVAF (d) NiCrBSi, APS, (e) NiCrBSi, HVOF, (f) NiCrBSi, HVAF

different powders by processes with different flame velocities and temperatures is assumed to affect the coating density and oxidation of particles during flight and thus the coating's corrosion behavior. In addition, NiCrBSi powder contains boron and carbon, which are known to bind some of the chromium in the alloy. The effect of the spray process on the microstructure has been presented in this study. The effect of structure on corrosion behavior of the coating is discussed in more detail below.

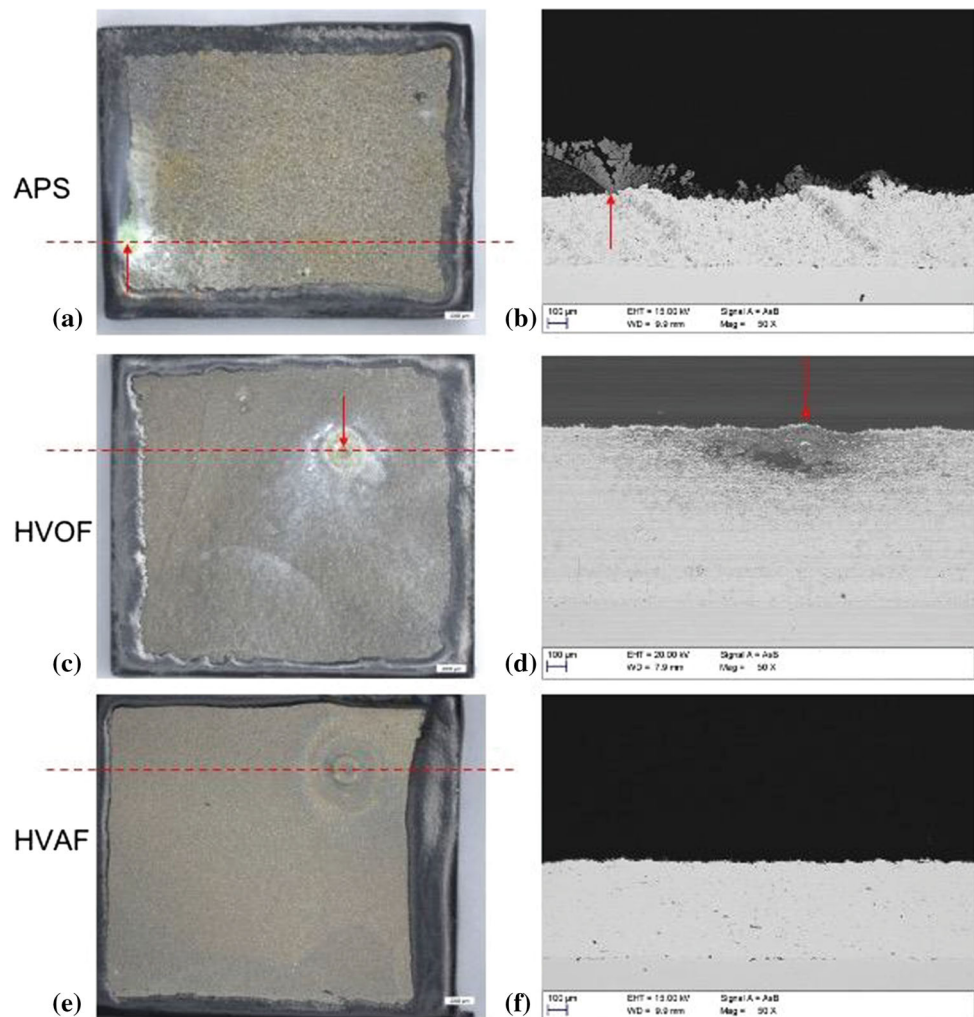
Electrochemical Behavior

The corrosion resistance of the studied coatings was lower than that of stainless steel 316. In general, the NiCr coatings performed better in NaCl solution than the NiCrBSi coatings. That can be assumed to be the effect of different chemical compositions of the coatings and, therefore the different resulting microstructure. NiCrBSi is a so-called fusible alloy (sprayed and fused), where in addition to the melting point lowering alloying elements, B and Si, 1% C is added. As a result, its microstructure contains chromium carbides/chromium boride precipitates (Fig. 2), which increase the hardness of the coating, but on the other hand, decreases the amount of Cr in the NiCr matrix and thus may impair its ability to form a chromium oxide layer effectively. That may cause the poorer corrosion resistance

of the NiCrBSi alloy compared to NiCr, which has an overall slightly higher Cr content and has no carbide formers.

The spraying method appeared to have some effect on the corrosion performance of coatings. It was evident that different spray processes resulted in different coating microstructures, which seemed to have a role in the corrosion behavior. Among NiCr coatings, the HVOF coating appears to be the best and APS the poorest, whereas for NiCrBSi coatings, the APS appears to be the best, and the corrosion resistance of the HVAF and HVOF coatings is almost equal. The behavior of the coatings in the electrochemical measurements indicates that the coatings tend to passivate in the chloride-containing environment used in this study. However, as-sprayed surfaces were heterogeneous, which has a negative effect on the repeatability of the measurements. The variable microstructures formed by the different deposition processes also affect the results obtained. These changes are related to the ability to form a protective oxide layer on the coating. For the NiCr samples the coatings differ with respect to the level of porosity and oxide formation. In APS coatings, porosity levels are the highest, and thick oxide strips are visible in the microstructure. Oxide strips visible around the lamellae bind the chromium, which lowers the amount of chromium in the matrix and reduces the possibility of the chromium forming a protective layer on the surface of the coating and

Fig. 9 NiCr coating test specimens and cross sections after immersion for ten weeks. Images (a, c, and e) are taken using stereomicroscope and (b, d, and f) are BSE images taken using SEM.

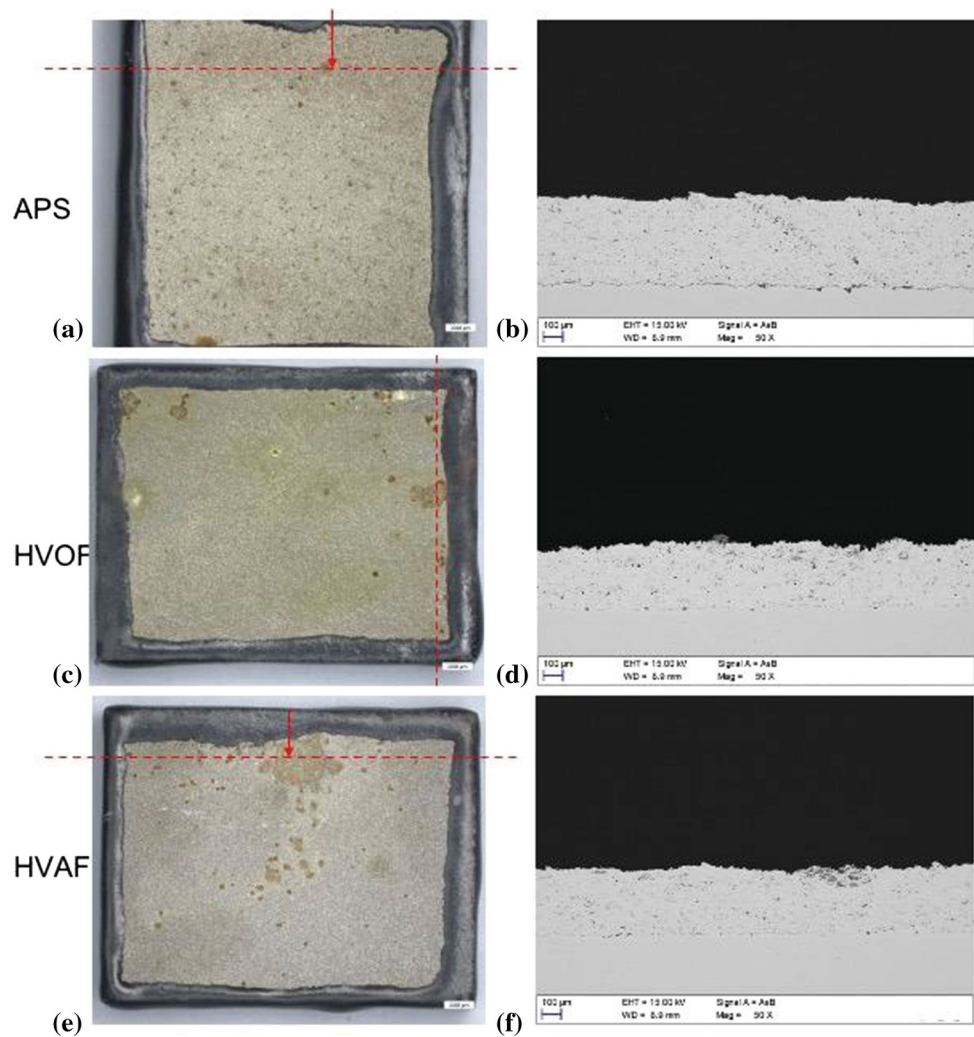


reduces corrosion resistance. It also appears that porosity or surface roughness might influence the electrochemical behavior of the coating. The corrosion performance of the HVOF NiCr coating may suffer from higher porosity than other methods. However, in one cyclic anodic polarization measurement in Fig. 7, the corrosion resistance of NiCr coating produced by HVOF was better than that of the stainless steel AISI 316, and it could be interesting to study these materials further in future studies. It can be emphasized here that when the coating oxidizes only slightly from the particle surface during spraying, i.e., does not deplete chromium by forming the chromium oxide, the corrosion resistance of the HVAF coating would be excellent. This is supported by other studies which show that compared to solid materials, the corrosion performance of thermally sprayed metallic coatings is typically poorer, but HVAF coatings show less of a reduction in corrosion performance compared to HVOF and APS coatings (Ref 4, 13, 18). However, since local corrosion was seen in the HVAF

NiCr coating during long-term exposures, which was related to local corrosion in pores, the coating structure was not yet optimal, as shown in Fig 1. Thus, it can be suggested that in this case, the corrosion resistance of the HVAF coating could be significantly improved by optimizing the coating process parameters or the barrel geometry. In addition, with a smaller powder particle size distribution, the porosity of the coating could be eliminated, and the corrosion-prone elements associated with porosity could be avoided. However, to avoid nozzle clogging, the above changes may require the use of ceramic nozzles, which are known to be available at the time of submission of this paper. In that case, the NiCr HVAF coating may have a high potential to be a corrosion protective coating in environments containing chlorides.

As discussed earlier, the NiCrBSi coatings showed different microstructures compared to the NiCr coatings. The microstructure related to the spray process temperature might explain the order of precedence of the coatings in

Fig. 10 NiCrBSi coating test specimens and cross sections after immersion for ten weeks. Images (a, c, and e) are taken by stereomicroscope and (b, d, and f) are BSE images taken using SEM



terms of corrosion resistance. The NiCrBSi APS coating has fewer precipitates, the HVAF and HVOF coatings, indicating that due to the higher flame temperature and lower flame velocity of the APS process, a higher fraction of powder has melted and chromium-binding precipitates in the powder have had the possibility to dissolve in the melt during spraying. Due to the high cooling rate of the splats, the chromium precipitates could not be precipitated back during cooling meaning that the chromium is in the matrix as a solid solution. On the other hand, many relatively round-shaped unmolten particles in the HVAF coating have the same microstructure as the original powder particles. Unmolten particles had chromium depleted regions next to Cr_3C_2 precipitate where the chromium cannot form the protective oxide layer and wherein the material is susceptible to selective corrosion of nickel. On the other hand, good corrosion properties of NiCrBSi APS coating can be explained by the increased Cr content of the matrix due to dissolution of chromium carbides during the spraying.

Corrosion in Immersion Test

The surfaces and cross sections of the coated specimens were examined for signs of corrosion, resulting from the 10 weeks of immersion in 3.5 wt.% NaCl solution. Some signs of corrosion were seen near the surface of the coatings. However, no signs of corrosion were found at the interface between the coating and the substrate either in electrochemical measurements or immersion tests. This indicates that corrosion occurs only at the surface of the coating, and there is no galvanic effect between the coating and the steel substrate. After ten weeks of immersion, mainly local corrosion appeared on the surfaces of some specimens, but no signs of chlorine at the coating-substrate interface were found. In the inspection of the cross sections of the coatings (Fig. 11), the effects of corrosion were observed in areas where the coatings had some discontinuities, e.g., defects. That indicates that local corrosion occurs on the surface because of the heterogeneous structure of the coating. The effects of local corrosion were most evident in NiCrBSi

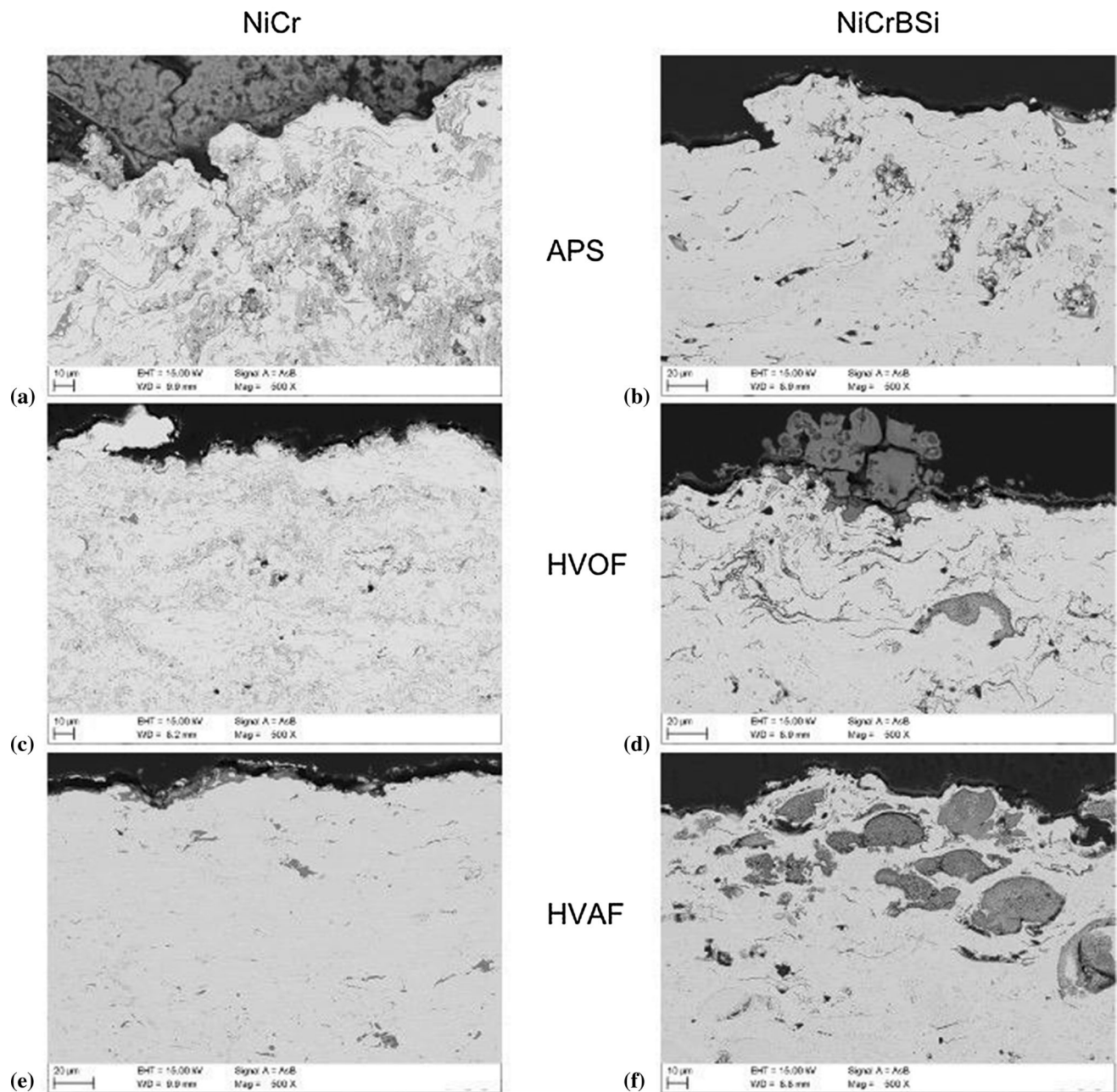


Fig. 11 Detailed BSE images of the immersion test specimens in Fig. 9 and 10 taken by SEM near the surface of the coating

coatings (Fig. 9), especially in HVAF NiCrBSi coating (Fig. 10). Figure 12 clearly shows that the unmolten particles in NiCrBSi are susceptible to corrosion. Therefore, it is likely that when chromium is bound to carbides or borides, the chromium-depleted zone around the carbide or boride will selectively corrode, leaving more noble chromium carbide or chromium-carbon-borides in the structure. That confirms the discussion of the previous chapter and, likely, that selective corrosion may not play as significant role if un-melted particles in the coating can be avoided.

Conclusions

In this study, the corrosion performance of thermally sprayed NiCr and NiCrBSi coatings sprayed by APS, HVOF, and HVAF processes was studied by means of open-circuit potential measurements, cyclic anodic polarization measurements, and immersion tests. In addition, the effect of the coating microstructure on the corrosion behavior was discussed. The following conclusions were made from this study:

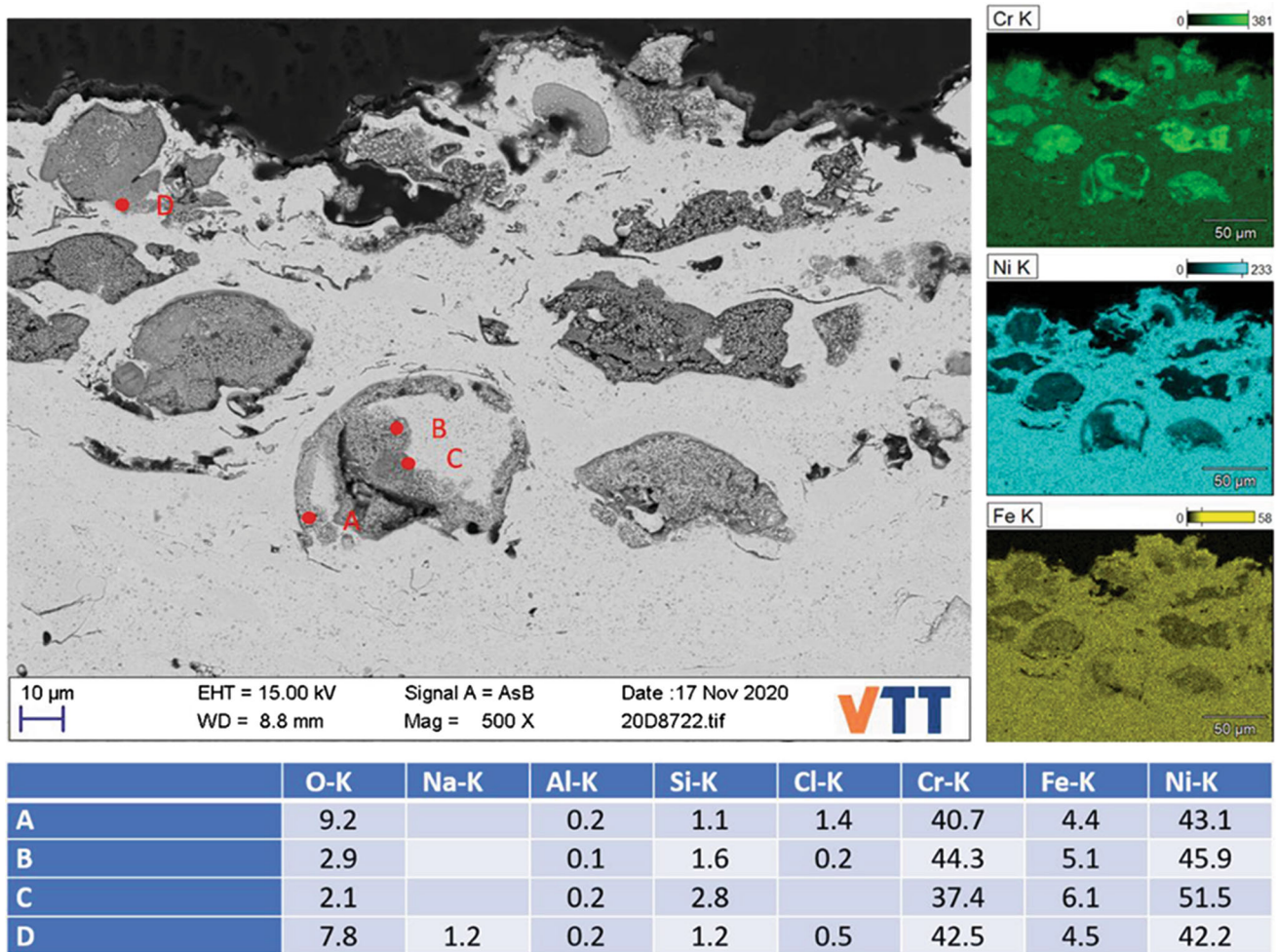


Fig. 12 A BSE image, EDS maps of chromium, nickel and iron, and the point analysis results at the corroded area in the NiCrBSi HVAF coating

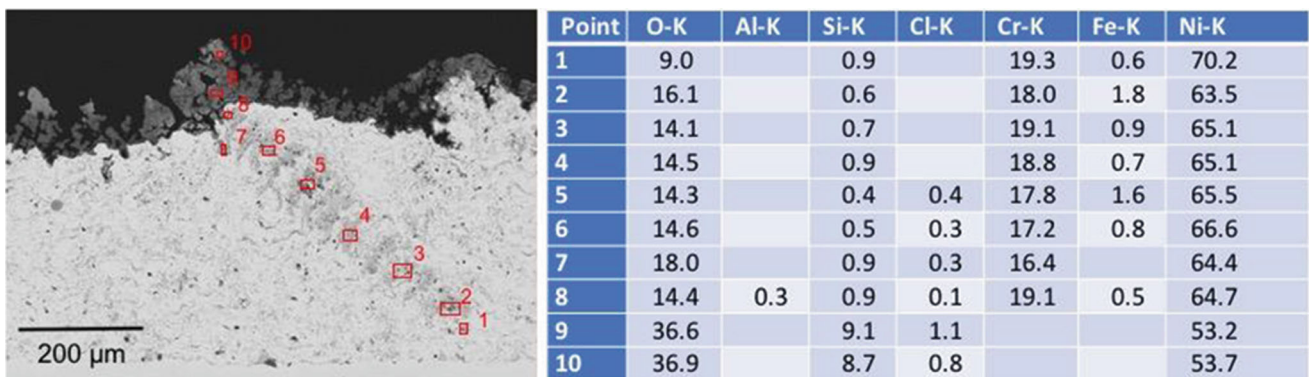


Fig. 13 EDS analysis results of NiCr APS coating at the point where corrosion was present on the surface of the specimen

- All coatings were dense enough to prevent the penetration of the chlorine ions to the coating-substrate interface
- The coatings tend to passivate in the aqueous NaCl environment.
- The NiCr coatings had better corrosion resistance than the NiCrBSi coatings.
- Differences between the spraying methods were marginal compared to the differences between the materials.

- For NiCr coatings, the HVOF coating appeared to have the best corrosion resistance in 3.5 wt.% NaCl solution and APS the poorest, whereas for NiCrBSi coatings, the APS performed the best. The corrosion resistance of the HVAF and HVOF coatings was almost equal in the 3.5 wt.% NaCl solution.
- Defects, voids, and other discontinuities in the microstructure reduced the corrosion resistance of the coating.
- Optimizing the spraying process and the powder particle size distribution may improve the corrosion resistance of the coating.

Funding This study was funded by Academy of Finland Project SA_HIERARCH - Enabling phenomena behind multihierarchical strengthening of high-kinetic sprayed metallic coatings. Open Access funding provided by Technical Research Centre of Finland (VTT).

Open Access This article is licensed under a Creative Commons Attribution 4.0 International License, which permits use, sharing, adaptation, distribution and reproduction in any medium or format, as long as you give appropriate credit to the original author(s) and the source, provide a link to the Creative Commons licence, and indicate if changes were made. The images or other third party material in this article are included in the article's Creative Commons licence, unless indicated otherwise in a credit line to the material. If material is not included in the article's Creative Commons licence and your intended use is not permitted by statutory regulation or exceeds the permitted use, you will need to obtain permission directly from the copyright holder. To view a copy of this licence, visit <http://creativecommons.org/licenses/by/4.0/>.

References

1. N. Papageorgiou, A. Von Bonin and N. Espallargas, Tribology International Tribocorrosion Mechanisms of NiCrMo-625 Alloy: An Electrochemical Modeling Approach, *Tribol. Int.*, 2014, **73**, p 177-186. <https://doi.org/10.1016/j.triboint.2014.01.018>
2. L.N. Moskowitz, Application of HVOF Thermal Spraying to Solve Corrosion Problems in the Petroleum Industry—an Industrial Note, *J. Therm. Spray Technol.*, 1993, **2**(1), p 21-29.
3. A. Neville, T. Hodgkiess and J.T. Dallas, A Study of the Erosion-Corrosion Behaviour of Engineering Steels for Marine Pumping Applications, *Wear*, 1995, **187**, p 497-507.
4. A. Neville, J.M. Perry, T. Hodgkiess and H.P. Chua, Wrought and High-Velocity Oxy Fuel Sprayed Inconel 625—Examination of Corrosion Aspects, *Proc. Inst. Mech. Eng.*, 2000, **214**(1), p 41-48.
5. S. Shrestha, A. Sturgeon, T. Hodgkiess and A. Neville, Corrosion Behaviour of High Velocity Oxy-Fuel (HVOF) Sprayed Ni-Cr-Si-B Coatings, *Thermal Spray 2002*. E. Lugscheider Ed., DVS, Essen, 2002
6. S. Shrestha, T. Hodgkiess and A. Neville, Erosion-Corrosion Behaviour of High-Velocity Oxy-Fuel Ni-Cr-Mo-Si-B Coatings Under High-Velocity Seawater Jet Impingement, *Wear*, 2005, **259**, p 208-218.
7. T. Hodgkiess, A. Neville and S. Shrestha, Electrochemical and Mechanical Interactions during Erosion-Corrosion of a High-Velocity Oxy-Fuel Coating and a Stainless Steel, *Wear*, 1999, **233**, p 623-634.
8. W.M. Zhao, Y. Wang, T. Han, K.Y. Wu and J. Xue, Electrochemical Evaluation of Corrosion Resistance of NiCrBSi Coatings Deposited by HVOF, *Surf. Coat. Technol.*, 2004, **183**(1), p 118-125.
9. E. Sadeghimeresht, N. Markocsan and P. Nylén, A Comparative Study on Ni-Based Coatings Prepared by HVAF, HVOF, and APS Methods for Corrosion Protection Applications, *J. Therm. Spray Technol.*, 2016, **25**(8), p 1604-1616.
10. E. Sadeghimeresht, N. Markocsan and P. Nylén, Microstructural Characteristics and Corrosion Behavior of HVAF- and HVOF-Sprayed Fe-Based Coatings, *Surf. Coatings Technol.*, 2017, **318**, p 365-373.
11. W.M. Zhao, Y. Wang, L.X. Dong, K.Y. Wu and J. Xue, Corrosion Mechanism of NiCrBSi Coatings Deposited by HVOF, *Surf. Coat. Technol.*, 2005, **190**(2-3), p 293-298.
12. P.H. Suegama, C.S. Fugivara, A.V. Benedetti, J. Fernández, J. Delgado and J.M. Guilemany, Electrochemical Behavior of Thermally Sprayed Stainless Steel Coatings in 3.4% NaCl Solution, *Corros. Sci.*, 2005, **47**(3 SPEC. ISS.), p 605-620.
13. E. Sadeghimeresht, N. Markocsan and P. Nylén, Microstructural and Electrochemical Characterization of Ni-Based Bi-Layer Coatings Produced by the HVAF Process, *Surf. Coat. Technol.*, 2016, **304**, p 606-619. <https://doi.org/10.1016/j.surfcoat.2016.07.080>
14. A.H. Dent, A.J. Horlock, D.G. McCartney and S.J. Harris, Microstructure Formation in High Velocity Oxy-Fuel Thermally Sprayed Ni-Cr-Mo-B Alloys, *Mater. Sci. Eng. A*, 2000, **283**, p 242-250.
15. A.H. Dent, A.J. Horlock, D.G. McCartney and S.J. Harris, The Corrosion Behavior and Microstructure of High-Velocity Oxy-Fuel Sprayed Nickel-Base Amorphous/Nanocrystalline Coatings, *J. Therm. Spray Technol.*, 1999, **8**, p 399-404.
16. A.H. Dent, A.J. Horlock, D.G.U. McCartney and S.J. Harris, Microstructural Characterisation of a Ni-Cr-B-C Based Alloy Coating Produced by High Velocity Oxy-Fuel Thermal Spraying, *Surf. Coat. Technol.*, 2001, **139**, p 244-250.
17. D. Chidambaram, C.R. Clayton and M.R. Dorfman, Evaluation of the Electrochemical Behavior of HVOF-Sprayed Alloy Coatings, *Surf. Coat. Technol.*, 2004, **176**, p 307-317.
18. N. Ahmed, M.S. Bakare, D.G. McCartney and K.T. Voisey, The Effects of Microstructural Features on the Performance Gap in Corrosion Resistance Between Bulk and HVOF Sprayed Inconel 625, *Surf. Coat. Technol.*, 2010, **204**(14), p 2294-2301. <https://doi.org/10.1016/j.surfcoat.2009.12.028>
19. G. Bolelli, D. Meschini, T. Varis, V. Testa, S. Morelli, L. Lusvarghi and P. Vuoristo, Corrosion Properties of Thermally Sprayed Bond Coatings Under Plasma-Sprayed Chromia Coating in Sulfuric Acid Solutions, *J. Therm. Spray Technol.*, 2020, **29**(1-2), p 270-284.
20. A. Milanti, H. Koivuluoto and P. Vuoristo, Influence of the Spray Gun Type on Microstructure and Properties of HVAF Sprayed Fe-Based Corrosion Resistant Coatings, *J. Therm. Spray Technol.*, 2015, **24**, p 1312-1322.
21. H. Koivuluoto, A. Milanti, G. Bolelli, L. Lusvarghi and P. Vuoristo, High-Pressure Cold-Sprayed Ni and Ni-Cu Coatings: Improved Structures and Corrosion Properties, *J. Therm. Spray Technol.*, 2014, **23**(1-2), p 98-103.
22. H. Koivuluoto and P. Vuoristo, Structure and Corrosion Properties of Cold Sprayed Coatings: A Review, *Surf. Eng.*, 2014, **30**(6), p 404-413.
23. H.R. Ma, J.W. Li, C.T. Chang, X.M. Wang and R.W. Li, Passivation Behavior of Fe-Based Amorphous Coatings Prepared by High-Velocity Air/Oxygen Fuel Processes, *J. Therm. Spray Technol.*, 2017, **26**(8), p 2040-2047.

24. Y. Wang, Z.Z. Xing, Q. Luo, A. Rahman, J. Jiao, S.J. Qu, Y.G. Zheng and J. Shen, Corrosion and Erosion-Corrosion Behaviour of Activated Combustion High-Velocity Air Fuel Sprayed Fe-Based Amorphous Coatings in Chloride-Containing Solutions, *Corros. Sci.*, 2015, **98**, p 339-353.
25. R.Q. Guo, C. Zhang, Q. Chen, Y. Yang, N. Li and L. Liu, Study of Structure and Corrosion Resistance of Fe-Based Amorphous Coatings Prepared by HVAF and HVOF, *Corros. Sci.*, 2011, **53**(7), p 2351-2356.
26. R. González, M.A. García, I. Peñuelas, M. Cadenas, M.R. Fernández, A.H. Battez and D. Felgueroso, Microstructural Study of NiCrBSi Coatings Obtained by Different Processes, *Wear*, 2007, **263**(1-6), p 619-624.
27. Š Houdková, E. Smazalová, M. Vost and J. Schubert, Surface & Coatings Technology Properties of NiCrBSi Coating, as Sprayed and Remelted by Different Technologies, *Surf. Coat. Technol.*, 2014, **253**, p 14-26.
28. J.M. Miguel, J.M. Guilemany and S. Vizcaino, Tribological Study of NiCrBSi Coating Obtained by Different Processes, *Tribol. Int.*, 2003, **36**(3), p 181-187.
29. E.R. Secosan, G. Marginean, R. Ciubotariu, Influence of the Fusing Process on the Wear and Corrosion Properties of NiCrBSi-Coatings, in *This Study the NiCrBSi Feedstock Powder Was Deposited by Flame* (1) (2015), pp. 385-397
30. S. Shrestha, T. Hodgkiess and A. Neville, The Effect of Post-Treatment of a High-Velocity Oxy-Fuel Ni-Cr-Mo-Si-B Coating Part 2: Erosion-Corrosion Behavior, *J. Therm. Spray Technol.*, 2001, **10**(4), p 656-665.
31. M. Oksa and J. Metsäjoki, Optimizing NiCr and FeCr HVOF Coating Structures for High Temperature Corrosion Protection Applications, *J. Therm. Spray Technol.*, 2015, **24**(3), p 436-453.
32. R. Jafari and E. Sadeghi, High-Temperature Corrosion Performance of HVAF-Sprayed NiCr, NiAl, and NiCrAlY Coatings with Alkali Sulfate/Chloride Exposed to Ambient Air, *Corros. Sci.*, 2019, **160**, p 108066.
33. Kermetico, <https://Kermetico.Com/Control-and-Auxiliary/Gas-Permeability-Tester-Thermal-Spray-Coatings-Porosity-Measurement>
34. A. Verstak, V. Baranovski, and M. Calkings, Critical Factors of Coatings Performance in Kraft Pulping Digesters, 1999
35. M. Oksa, S. Tuurna and T. Varis, Increased Lifetime for Biomass and Waste to Energy Power Plant Boilers with HVOF Coatings: High Temperature Corrosion Testing Under Chlorine-Containing Molten Salt, *J. Therm. Spray Technol.*, 2013, **22**, p 783-796.
36. G. Bolelli, L. Lusvarghi and R. Giovanardi, A Comparison Between the Corrosion Resistances of Some HVOF-Sprayed Metal Alloy Coatings, *Surf. Coat. Technol.*, 2008, **202**(19), p 4793-4809.

Publisher's Note Springer Nature remains neutral with regard to jurisdictional claims in published maps and institutional affiliations.